



OPEN Experimental study on the splitting tensile failure of a carbon nanotube-modified fly ash foamed concrete filler

Shukun Zhang¹, Xinghui Wu¹✉, Peng Jiang¹, Haohao Wang¹, Shuai Wang¹, Haojie Yang² & Lu Lu¹

To study the enhancement effect of carbon nanotubes (CNTs) on the splitting tensile properties of foamed concrete backfill in which cement and fly ash were used as the cementitious materials and natural sand was used as the aggregate, specimens of CNT-modified foamed concrete backfill were prepared. Brazilian splitting tests were used to investigate the splitting tensile strength of the CNT-modified foamed concrete backfill, and the digital speckle correlation method was used to analyze the stress field characteristics and crack expansion law of the specimens during splitting tensile testing. The stress–strain characteristics and energy dissipation laws of the backfill were studied at various static loading rates, and a relationship between the splitting tensile strength, ultimate strain, and loading rate was established. The results showed that at the optimum CNT content of 0.05%, the peak strength and ultimate strain of the modified foamed concrete backfill increased by an average of 67.2% and 21.7%, respectively. Moreover, after modification with CNTs, the foamed concrete backfill was less likely to develop strain concentration areas before reaching peak strength. The triangular stable loadbearing structure formed by the modified foamed concrete backfill after splitting caused the end of the stress–strain curve to exhibit varying degrees of “backlash”. For the CNT-modified foamed concrete backfill, the peak strength correlated logarithmically with the loading rate, while the ultimate strain correlated as a power function of the loading rate. At a low loading rate, the CNT-modified foamed concrete backfill dissipated less energy, and the reverse was true for higher rates.

Keywords CNTs, Foamed concrete, Backfill, Splitting tensile, Loading rate, Energy dissipation

Foamed concrete, with its unique pore structure, is renowned for its lightweight properties and superior thermal insulation, shock absorption, and pressure relief capabilities¹. It has been widely adopted in various construction applications, including wall insulation, flooring, and as a filling material in mining operations, due to its environmental benefits and cost-effectiveness. The use of fly ash in foamed concrete not only enhances the stability and environmental performance but also contributes to the sustainable utilization of industrial by-products. The incorporation of fly ash and bubbles in foamed concrete reduces costs and increases the fluidity of the mixed slurry, making it a potential material for ore body filling. Despite these advantages, the low strength characteristics of traditional backfill have limited the broader application of foamed concrete. Recent studies have shown that the addition of fibers, including carbon nanotubes, can significantly improve the mechanical properties of foamed concrete, opening new avenues for research and development in this field^{2–5}.

Traditional basalt fibers, polypropylene fibers, metal fibers, and linen fibers have strong tensile properties. Due to the bridging effect of fibers between the cement matrix, the expansion of cracks in foamed concrete can be suppressed at a macroscale^{6–10}. To date, a large number of scientific researchers have also started to use “non-macrofibers” (i.e., fibers that are smaller than macroscale) or particles to improve the mechanical properties of concrete, and research has achieved fruitful results^{11,12}. For example, Zhang et al. experimentally verified that carbon nanotubes (CNTs) have a certain strengthening effect on the compressive strength and splitting strength of concrete¹². Liu et al. prepared hydroxylated boron nitride (h-BN-OH) using a chemical modification method to enhance its potential application in cement-based materials¹³. Onaizi et al. studied the properties of furnace bottom ash (FBA) and its use in cementitious composites, identifying potential applications, environmental

¹School of City and Architecture Engineering, Zaozhuang University, Zaozhuang 277160, Shandong, China. ²School of Civil Engineering, Liaoning Technical University, Fuxin 123000, Liaoning, China. ✉email: wuxinghui92@163.com

| Material type | Morphology | Purity (%) | Grey (%) | Diameter (nm) | Tube length (μm) | Specific surface area | Bulk density (g/cm^3) |
|---------------|--------------|------------|----------|---------------|-------------------------------|-----------------------|---|
| MWCNTs | Black powder | >97 | <2.5 | 3–15 | 15–30 | 250–270 | 0.06–0.09 |

Table 1. Material parameters of the CNTs.

| Number | Factor | | | | |
|--------|------------|--------------|---------------|---------|-------------------------|
| | Fly ash(%) | Bone glue(%) | Water glue(%) | CNTs(%) | Foam volume fraction(%) |
| 1 | 40 | 0 | 45 | 0 | 50 |
| 2 | 60 | 5 | 50 | 0.05 | 80 |
| 3 | 80 | 10 | 55 | 0.10 | 120 |
| 4 | 100 | 15 | 60 | 0.15 | 150 |

Table 2. The mixing proportion table.

benefits, and cost feasibility¹⁴. These “non-macrofibers” or particles can inhibit the initiation of cracks, and improving the mechanical properties of concrete is a future development trend for fibers¹⁵.

The initiation, expansion and coalescence of the cracks in foamed concrete are essentially tensile cracks or shear cracks in the cement^{16–19}. At present, research on improving the performance of foamed concrete through microfiber modification has not been carried out in large quantities. Shahpari et al. studied the effect of CNTs on the fire resistance of foamed concrete²⁰. In a recent study by Abd, the potential of integrating nanosilica (NS) into ultra-lightweight foamed concrete (ULFC) with an oven-dry density of $350 \text{ kg}/\text{m}^3$ was explored, focusing on the fresh and hardened properties of the material²¹. Nano-silica, also known as silica nanoparticles, is a pozzolanic material that has been widely used to improve the properties of cementitious materials. It is known for its high specific surface area and reactivity, which accelerates the hydration process and enhances the mechanical properties of concrete. The addition of nano-silica has been reported to increase the compressive and flexural strength of cement paste due to the formation of additional C-S-H gel from the pozzolanic reaction. It also improves the thermal stability of the cementitious system and reduces calcium leaching. Sldozian’s research delves into the effects of carbon nanotube (CNT)-based modifiers on the performance characteristics of lightweight foamed concrete (LFC)²². Carbon Nanotubes (CNTs) have been recognized for their potential to enhance the mechanical properties of LFC. The incorporation of CNTs in LFC can lead to a significant improvement in tensile strength and toughness due to their high aspect ratio and excellent mechanical properties. CNTs can bridge micro-cracks, preventing their propagation and enhancing the overall durability of the material. Recent studies have shown that the addition of CNTs can improve the modulus of elasticity and hardness of cement paste, and increase the compressive strength of cement paste by 20–25% with 0.5–2% addition of nano-silica by weight of cement. Beyond 2% addition, a reduction in strength is noticed. In the context of LFC, CNTs can form a percolation network within the cement matrix, which significantly affects the electrical and thermal conductivity of the material. The presence of CNTs also improves the durability of LFC by reducing water absorption and enhancing resistance to chemical.

In this paper, the foamed concrete used for mining and filling is taken as the research object, and the modified foamed concrete is prepared by using a small number of CNTs. The Brazilian splitting test was used to investigate the stress–strain relationship and splitting tensile properties of CNT-modified foamed concrete, and the digital speckle correlation method (DSCM) was used to analyze the characteristics of the strain field and crack propagation during the cleavage process. The stress–strain characteristics and energy dissipation laws of CNT-modified foamed concrete under different loading rates were studied, the functional relationship between the splitting strength, ultimate strain and loading rate was established, and the mechanism of splitting failure in CNT-modified foamed concrete backfill was revealed.

Test materials and methods

Test materials

Cement and fly ash were used as cementitious materials, natural sand was used as aggregate, and modified foamed concrete was prepared by microdosing CNTs. The cement was used PO42.5 Portland cement, which was produced by Fuxin Daying Cement Manufacturing Co., Ltd., while the fly ash was produced by the Fuxin thermal power plant. For the cementitious materials, the density was $2.0 \text{ g}/\text{cm}^3$ and the fineness was 10.8% by weight. The natural river sand had a particle size of less than 2.4 mm and an apparent density of $2.2 \text{ g}/\text{cm}^3$. The foaming agent was produced by Zhengzhou Pengyi Chemical Products Co., Ltd.. The CNTs were produced by Shenzhen Turing Evolution Technology Co., Ltd, and the material parameters of these CNTs are detailed in Table 1.

Preparation of test specimens

The cement, fly ash, natural sand, and water were fully mixed according to the design ratio (Table 2), thereby creating a homogeneous slurry mixture. The CNT suspension was prepared by 5 min of mechanical agitation followed by 30 min of ultrasonic dispersion. The liquid foaming agent and water were mixed into a container at a ratio of 1:40 and then mechanically stirred to prepare a uniform and stable foam. The slurry mixture, CNT

suspension, and foam were mixed thoroughly in this order and stirred for 10 min, and then a cylindrical foam concrete specimen with a diameter of 5 cm and a height of 10 cm was poured.

Test methods

Test plan

The proportion of foamed concrete materials was initially determined to ensure the uniaxial compressive strength met the requirements for filling and mining. The specific mass ratios for the materials are as follows: the mass ratio of the fly ash to cement is 80%, the mass ratio of the natural sand to cementitious materials is 10%, and the mass ratio of the water to cementitious materials is 45%. Foamed concrete test pieces were prepared with CNT-to-cementitious material ratios of 0%, 0.05%, 0.10%, and 0.15%, and 3 parallel specimens were prepared for each mix ratio; thus, 12 test pieces were prepared for the 4 mix ratios. The tensile stress–strain relationship of the test specimens was tested for splitting, and the optimal CNT-to-cementitious material ratio in the foamed concrete was determined through an analysis of the sample deformation and failure under loading. The test specimen with the optimal CNT-to-cementitious material ratio was subjected to splitting tensile tests with loading rates of 0.1 mm/min, 0.5 mm/min, 1.0 mm/min, 1.5 mm/min, and 2.0 mm/min. For each loading rate, three replicate samples were tested to ensure statistical reliability. This experimental design resulted in a total of 15 samples being tested, allowing for a comprehensive analysis of the deformation and failure characteristics of the CNT-modified foam concrete under varying loading conditions.

Test equipment parameters

The splitting tensile test was performed with a TAW2000 rock mechanics testing machine, and the loading rate for the test with the optimal ratio was controlled at 1.0 mm/min. When the loading rate was affected, the loading rate of the testing machine was adjusted according to the design requirements. The ultrasonicator, model AK-008A, had an ultrasonic frequency of 40 kHz and a power output of 600 W. A handheld mixer (model Gomez) was used to mix the slurry and foam and the stirring speed was set to 1500 r/min.

Test method

The Brazilian test is the simplest and most effective test method for measuring the tensile strength of brittle materials, such as rock and concrete, however, point loading and splitting easily cause stress concentrations. Therefore, the Brazilian splitting test is used to test the splitting tensile strength of the specimen. The disc-shaped specimen was placed on the pressure platform of the testing machine, and a tensile stress in the radial direction was generated by applying diametric compression to determine the tensile strength. In this test, the thickness-to-diameter ratio was 1.0, and the splitting angle was $2\beta = 30^\circ$. The splitting tensile strength σ_t can be calculated according to Eq. (1).

$$\sigma_t = \frac{-2P \sin \beta \cos^2 \beta}{\pi DL(\sin \beta \cos \beta - 2\beta)} \quad (1)$$

where L is the thickness of the processed specimen, D is the diameter of the specimen, and P is the failure load. The DSCM was used to observe the splitting tensile test process. The DSCM tracked and identified the trajectory of the initial speckle pattern on the specimen surface during the loading process to obtain the surface deformation. As shown in Fig. 1, the first picture captured by the DSCM is the reference image I_0 , whereas the series of captured images following the loading process are distorted images. If point A in the reference image I_0 is used as the analysis object, the target image I_t at a corresponding time in a series of deformed images can be extracted. Then, a characteristic speckle pattern at point B that matches that at point A can be determined. The difference in the amount of deformation between points A and B is the deformation value at point A. In the speckle pattern method, point A represents the initial position of a speckle pattern on the specimen's surface in the reference image (I_0), while point B corresponds to the position of the same speckle pattern after deformation in the target image (I_t). The correlation function compares these two points to determine the displacement and deformation of the specimen's surface under load. The highest correlation value indicates the best match between the initial and deformed speckle patterns, providing precise measurements of the material's response to the applied stress. The degree of matching between f and g is characterized by the correlation function C . When C takes the maximum value, it is represented as the best match, as shown in Eq. (2).

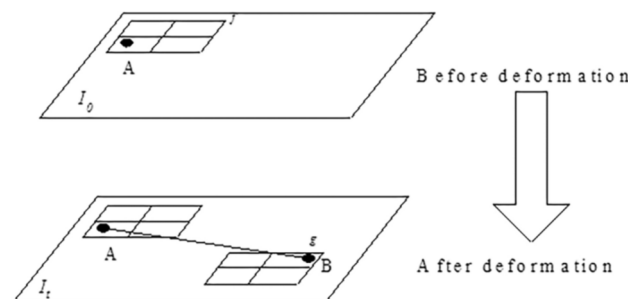


Fig. 1. Deformation of the DSCM observation target.

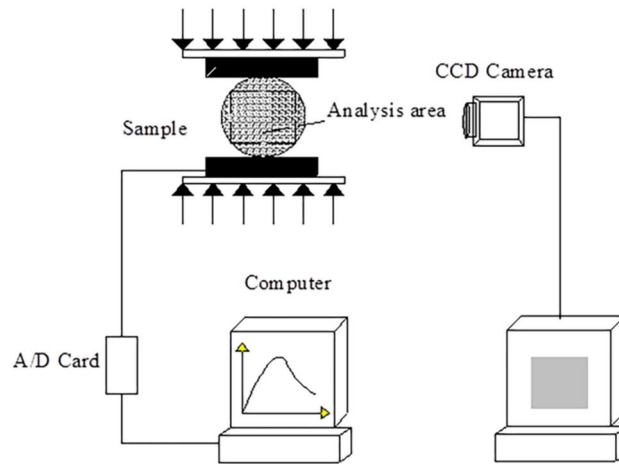


Fig. 2. Test process.

| CNTs % | Specimen number | Tensile strength/MPa | Average tensile strength/MPa |
|--------|-----------------|----------------------|------------------------------|
| 0 | 1-1 | 0.398 | 0.403 |
| | 1-2 | 0.412 | |
| | 1-3 | 0.400 | |
| 0.05 | 2-1 | 0.680 | 0.674 |
| | 2-2 | 0.645 | |
| | 2-3 | 0.697 | |
| 0.10 | 3-1 | 0.712 | 0.711 |
| | 3-2 | 0.698 | |
| | 3-3 | 0.724 | |
| 0.15 | 4-1 | 0.704 | 0.719 |
| | 4-2 | 0.722 | |
| | 4-3 | 0.731 | |

Table 3. Splitting tensile strength.

$$C = \frac{\sum \{ [f(x, y) - \bar{f}] [g(x', y') - \bar{g}] \}}{\sqrt{[f(x, y) - \bar{f}]^2} \sqrt{[g(x', y') - \bar{g}]^2}} \quad (2)$$

where $f(x, y)$ and $g(x', y')$ are gray functions of a small area and \bar{f} and \bar{g} are the average values of $f(x, y)$ and $g(x', y')$, respectively.

The Brazilian splitting test was performed while the CCD camera recorded images of the sample surface; the resolution of the CCD camera was 1630×1224 pixels. For the low-density foamed concrete surfaces, the speckle field needs to be manually sprayed so that the camera can capture the surface deformation information of the specimen. The speckled specimen was set on a loading platform, and the orientation of the CCD camera was corrected to capture the entire area of the end face of the specimen. The speckle calibration resolution was 0.05 mm/pixel, and the image acquisition frequency was 2 fps. The test process is shown in Fig. 2. The analysis area is a rectangle inscribed on the circular surface of the specimen, and the aspect ratio is 4:3.

Analysis of test results

Determination of the optimal mixing amount for the modified foamed concrete

Determination of the optimal ratio

The splitting tensile strength test data are shown in Table 3.

Table 2 shows that as the CNT content increases, the tensile strength of the foamed concrete increases significantly. In particular, the incorporation of a CNT content of 0.05% increased the average tensile strength the concrete by 67.2%. When the proportion of CNTs increased to 0.10% and 0.15%, the tensile strength increased by 5.5% and 1.1%, respectively. Excessive incorporation of CNTs resulted in agglomeration, which reduced the bridging behavior between CNTs and the foamed concrete matrix. The agglomerated area became a weak area of tensile strength, which is similar to the responses reported in other fiber-modified concrete. A higher CNT

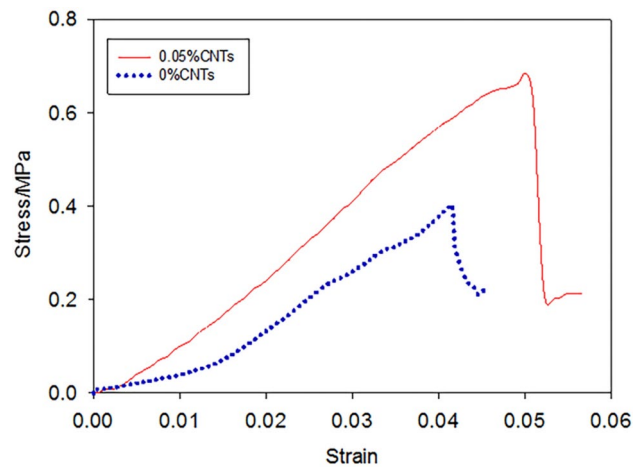


Fig. 3. Tensile stress–strain curves of the foamed concrete before and after modification.

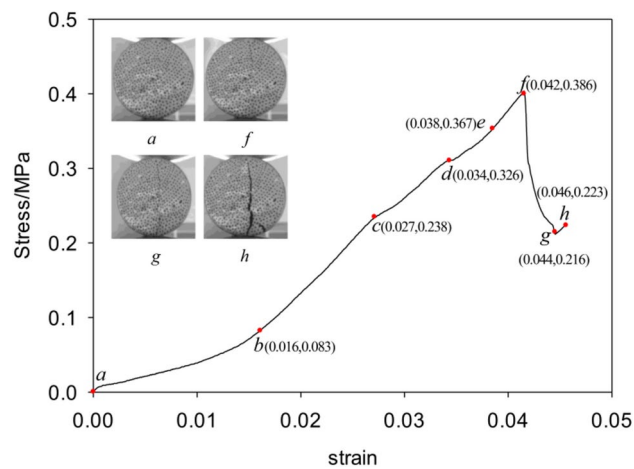


Fig. 4. Stress–strain curve and characteristic failure points of the foamed concrete before modification.

content significantly increased the cost but did not contribute significantly to the splitting tensile strength of foamed concrete. Therefore, it was determined that the optimal CNT content is 0.05%.

Comparative analysis of the stress–strain curves of the foamed concrete before and after modification

The stress–strain curves of specimens 1–3 and 2–1, which had splitting tensile strength values closest to the average strength of this group, were extracted from the foamed concrete specimens with CNT blending ratios of 0% and 0.05%, as shown in Fig. 3.

From the perspective of the overall stress–strain curve, the specimens underwent an initial compaction stage, a linear elastic deformation stage, a plastic deformation stage, and a splitting instability stage. The specimens do not exhibit ductility similar to the postpeak curve of uniaxially compressed foamed concrete, indicating that the tensile properties of the specimen are close to brittleness. The splitting tensile strength of the unmodified foamed concrete is 0.40 MPa, the strain corresponding to the peak strength is 0.040, and the ultimate strain is 0.046. The splitting strength of the modified foamed concrete is 0.68 MPa, the strain corresponding to the peak strength is 0.048, and the ultimate strain is 0.056. Therefore, the peak strength of the modified foamed concrete increased by 70.0%, the strain corresponding to the peak strength increased by 20%, and the ultimate strain increased by 21.7%. The incorporation of CNTs significantly improved the tensile strength and tensile deformation. This finding shows that under an external load, CNTs can effectively suppress the initiation of cracks at the mesoscale. The peak strength trailing curve is still falling, indicating that once the cracks initiate and expand after continued loading, the CNTs have no constraint on the crack resistance. The postpeak curve strain range is small, and there is not much difference before and after modification.

Comparative analysis of the horizontal strain in the foamed concrete before and after modification

As shown in Fig. 4, the characteristic points are marked on the stress–strain curve of the foamed concrete before modification, in which a is the starting point, b is the end of the compaction stage, c is the yield stage point 1, d

is the yield stage point 2, e is the yield stage point 3, f is the peak point, g is the lowest point of the curve stress after the peak, and h is the endpoint. The fracture maps corresponding to e, f, g, and h are extracted and displayed in Fig. 4. The specimen in Fig. 4(a) is in the initial state, and the peak specimen in Fig. 4(f) corresponds to macrocracks. Figure 4(g) corresponds to the complete longitudinal fracture of the test specimen, in which the test specimen was split into two parts. Moreover, as the longitudinal crack penetrated point (h) in Fig. 4, a small piece of crushing occurred again at the lower end point, and the stress–strain curve had a significant “backlash”, after which the specimen was completely destroyed.

The characteristic points are marked on the splitting tensile stress–strain curve of foamed concrete, and the failure deformation information obtained by combining the relevant point failure specimens is not sufficiently comprehensive. As shown in Fig. 5, the speckle cloud of horizontal strain corresponding to the characteristic points on the stress–strain curve was extracted to further analyze the evolution law of the horizontal strain field on the surface of the specimen during the splitting process.

In the process of compressing the specimen in the radial direction, it is equivalent to the tensile action in the horizontal direction. The tensile force is positive, and the pressure is negative. Figure 5(a) shows the horizontal strain field corresponding to the unloaded specimen, the cloud distribution is irregular, and the specimen deformation is in the initial state. Figure 5(b) shows the horizontal strain field corresponding to the specimen in the elastic stage. The horizontal strain value increased slightly, but the distribution still had no obvious tensile trend. Although the horizontal strain value of the strain field in Fig. 5(c) is not large, the cloud distribution of the strain field exhibited a certain trend. In the vertical direction, there were multiple red areas with a concentration of 3×10^{-3} . The horizontal strain field distribution in Fig. 5(d) and Fig. 5(e) was clear. However, the upper and lower vertices of the specimen in contact with the testing machine were deformed first, and the strain concentration area reached 6×10^{-3} ; thus, the internal horizontal strain value for the specimen did not change much. Although a Brazilian platform loading test was used herein, the deformation at this location was still mainly provided by the deformation of the specimen at the contact point with the testing machine. This phenomenon also explains why many scholars believe that the stress concentration caused by the Brazilian splitting test under point loading makes the tensile strength test inaccurate. Under continuous loading, the specimen quickly reached its ultimate loadbearing capacity, as shown in Fig. 5(f). Under continuous loading, the evolution of the strain concentration area nearly finished its expansion rapidly, and the strain concentration zone expanded from the center of the specimen. If the specimen had poor uniformity, the stress concentration zone may spread from the edge. The strain value in the strain concentration zone formed by the tension was between 0.02 and 0.05, the strain value had an order of magnitude leap, and a through crack developed in the sample. As shown in Fig. 5(g), the strain concentration band of the specimen penetrated the upper and lower vertices of the specimen, the strain value was between 0.05 and 0.25, and specimen had already been damaged. As shown in Fig. 5(h), the fully expanded cracked specimen did not immediately lose stability, and the local strain of the cracked specimen was -0.4, which corresponds to the end point of the stress–strain curve. The results show that the specimen formed a temporarily stable structure and was crushed again until the failure became unstable. The characteristic points of the stress–strain curve were extracted and analyzed according to the analysis method used for the foamed concrete before modification. The boundary of the stress–strain curve before the peak strength of the modified foamed concrete was not obvious, and it did not reflect the obvious compaction stage, elastic deformation and yield deformation stage. To facilitate comparison, the characteristic points of the curve in Fig. 5 were normalized according to Eq. (3) and (4). Then, the peak strength curves a, b, c, d, and e were divided by the peak strain ε_f corresponding to the peak strength at the characteristic point strain curve ε_i ($i = a, b, c, d, \text{ and } e$) of the specimen

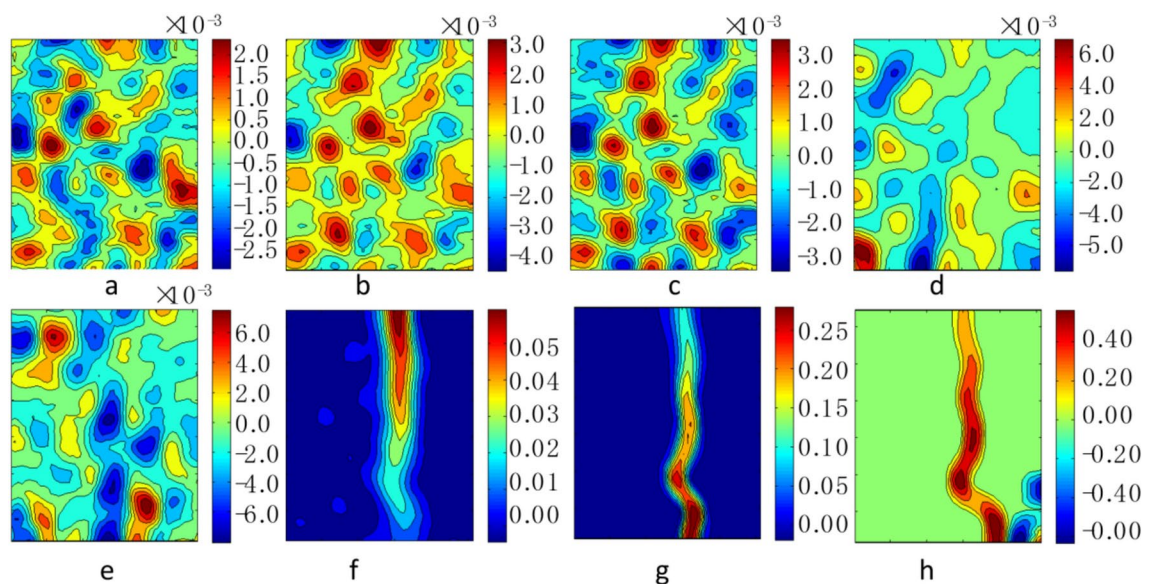


Fig. 5. Horizontal strain field at the characteristic points of the foamed concrete before modification.

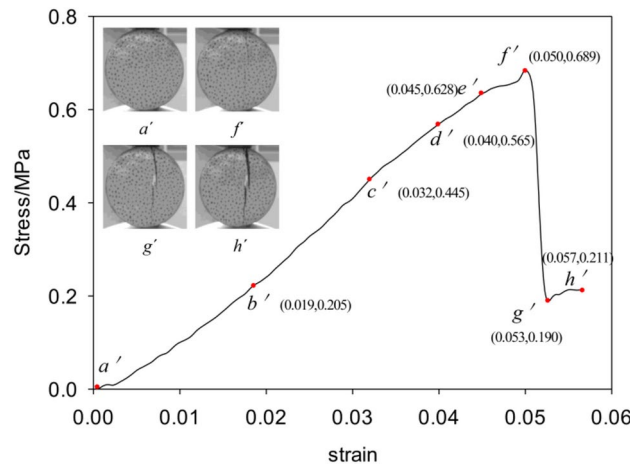


Fig. 6. Stress–strain curve and characteristic failure points of the modified foamed concrete.

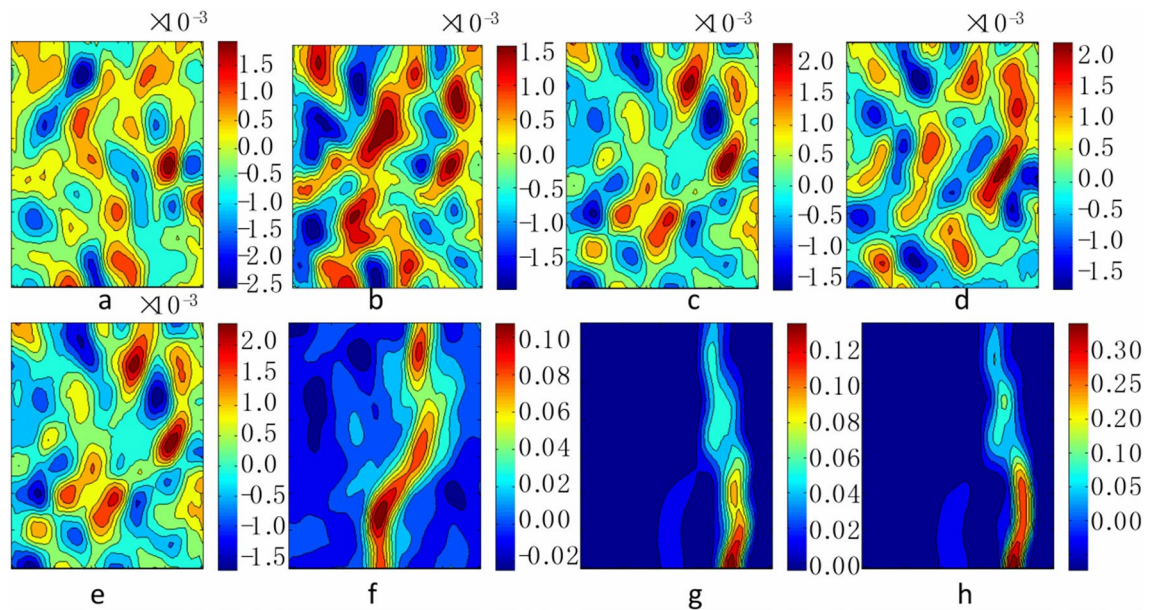


Fig. 7. Horizontal strain field at the characteristic points of the modified foamed concrete.

before modification in Fig. 4. The normalized coefficient η_i was multiplied by the peak strain $\eta_{f'}$ corresponding to the peak strength of the modified stress–strain curve to obtain the corresponding strain value η_i ($i = a, b, c, d,$ and e), and the stress after modification is the corresponding $a', b', c', d',$ and e' ; feature points marked on the strain curve.

$$\eta_i = \varepsilon_i / \varepsilon_{f'} \quad (i = a, b, c, d, e) \tag{3}$$

$$\varepsilon_i = \eta_i \bullet \varepsilon_{f'} \quad (i = a, b, c, d, e) \tag{4}$$

Note that g' and h' still correspond to the lowest point of the postpeak curve stress value and the end point of the postpeak curve, as shown in Fig. 6. The specimen at point a' in Fig. 6 is in the initial state, and the peak point graph f' corresponds to two macrocracks near the penetration. Point g' corresponds to the coalescence of two longitudinal cracks in the specimen, and the specimen is split into two parts. Moreover, when point h' penetrates through the longitudinal crack, the macrocrack is further opened; however, there is no phenomenon similar to the failure of the lower end of the unmodified specimen. There is also a certain degree of “backlash” at the end of the stress–strain curve, but it is not as obvious as the stress–strain curve of the specimen before modification.

As shown in Fig. 7, the horizontal strain scatter cloud pattern corresponding to the characteristic points on the stress–strain curve is extracted to further analyze the evolution law of the horizontal strain field on the surface of the specimen during the splitting process.

Figure 7(a) shows the horizontal strain field corresponding to the unloaded specimen, and the deformation of the specimen is in the initial state, which is consistent with the unmodified specimen. Figure 7(b) shows the corresponding horizontal strain field of the specimen in the elastic stage. The maximum horizontal strain area is 1.5×10^{-3} . Figure 7(c), Fig. 7(d) and Fig. 7(e) show little difference in strain values, but the distribution shows a clear trend of strain concentrations. The local horizontal strain in the specimen is approximately 2.5×10^{-3} , which is 41.7% ~ 83.3% of that in the unmodified specimen. As shown in Fig. 7(f), under continuous loading, the strain value in the strain concentration band formed by the internal tension of the specimen is between 0.02 and 0.1. A through crack was formed in the specimen at an instant, reaching the peak strength, and the strain concentration band caused by tensile cracking began in the central region. As shown in Fig. 7(g), the strain in the central region reaches 0.04, whereas the strain in the edge reaches 0.12. This phenomenon occurs because under continuous loading, according to the geometric relationship, the deformation of the tensile crack notch is greater at the edge than in the central region, and the corresponding strain value is also larger. If this process is not captured with a high-speed camera, the illusion that the edge cracks first is often obtained, and experimental results that contradict the theory are obtained. Heterogeneous rock masses, concrete and other materials, especially with obvious notches and cracks, exhibit different behavior. The load continues to increase until the specimen becomes unstable and fails, as shown in Fig. 7(h). The fracture is completely penetrating and unstable, and the horizontal strain value reaches 0.30. There is no obvious secondary strain concentration zone in the specimen, but the specimen still maintains a short-term stability after splitting, and the corresponding stress–strain curve has a certain degree of “backlash” phenomenon. In the analysis of the horizontal strain field of the specimen before and after modification, the area of the horizontal strain concentration in the modified rock sample is slightly smaller than that in the unmodified sample in the initial compaction stage, steep deformation increase stage, and splitting instability stage. However, these values are not much different. The strain concentration band caused by crack propagation starts from the central area of the specimen, which is consistent with the traditional theory^{23,24}.

Fissure propagation characteristics

Concrete and rock are brittle materials. When the tensile strength of the Brazilian splitting test specimen is reached, the data measured when the center crack is reached are more meaningful (Zhao, Ma, et al. 2020; Luo et al. 2017). Heterogeneous rocks, concrete and other brittle materials have cracks, defects and different loading methods, which will cause the edges of the test specimen to crack and distort the test results. To make the splitting tensile test representative in this paper, the specimens were as uniform as possible, and a 30° loading angle was used (Saridemir 2016; Komurlu et al. 2016).

The crack propagation process of the foamed concrete specimens with a CNT content of 0.05% is shown in Fig. 8. The cumulative deformation stage is shown in Fig. 8(a). There is no crack on the surface of the test piece. The compression of the opposite diameter causes the specimen to produce vertical radial compression and horizontal radial elongation. The vertical deformation is mainly composed of the plastic compaction deformation of the pores of the specimen, the elastic deformation of the material particles, and the plastic closing deformation of the internal cracks; macroscopic cracks have not occurred. The stage of stable fracture expansion is shown in Fig. 8(b), 8(c), and 8 (d). In Fig. 8(b), two macrocracks appeared quickly and extended from the center to the edge of the specimen. Figure 8(c) shows that as the loading continued, the two cracks extended towards the vertex and bottom point of the loading platform and had a tendency to penetrate. Figure 8(d) shows that as the loading further increased, the two cracks penetrated and extended to the edge of the specimen. The stage of cracking is shown in Fig. 8(e). The crack penetrated the sample in Fig. 8(d), but the specimen can still withstand the applied load and reach the state shown in Fig. 8(e).

As shown in Fig. 8(e), the damage mainly manifests as macrocracks, and the size of the edge cracks is several times the size of the center crack. The structure formed after the specimen is split is drawn as a schematic diagram in Fig. 9. The loading continued to increase until the specimen splits, at which point the deformation reaches the maximum value and the stress reaches the lowest point. The two parts (I and II) formed by the splitting constitute a triangular stable structure, which makes the specimen enter a short rebalanced state. As parts I and II are further loaded, the phenomenon of “backlash” appeared at the end of the stress–strain curve. The rebalancing of this triangular stable structure is brief. The stable structure formed by parts I and II is instantly pressure-fed, and the specimen loading ends. Figure 9(a) shows that the specimen is not completely split, and Fig. 9(b) shows that the specimen is completely split into parts I and II. According to the geometric relationship, the maximum opening size n is at least twice the center opening m . If the image information of the

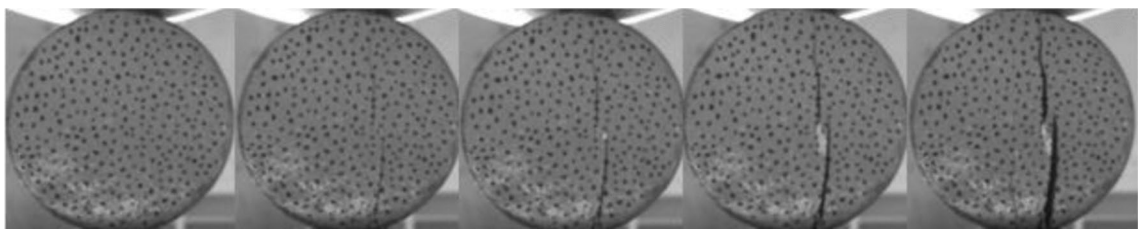


Fig. 8. Crack propagation process.

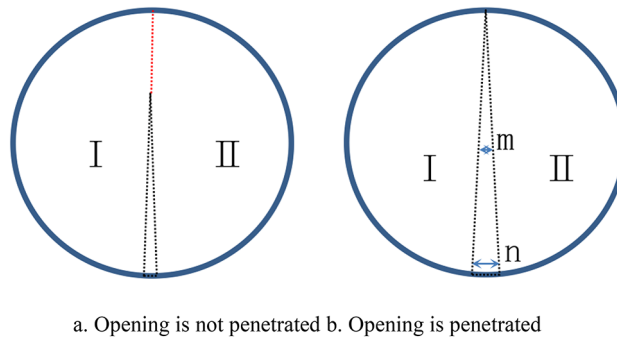


Fig. 9. Schematic diagram of the split structure of the specimen.

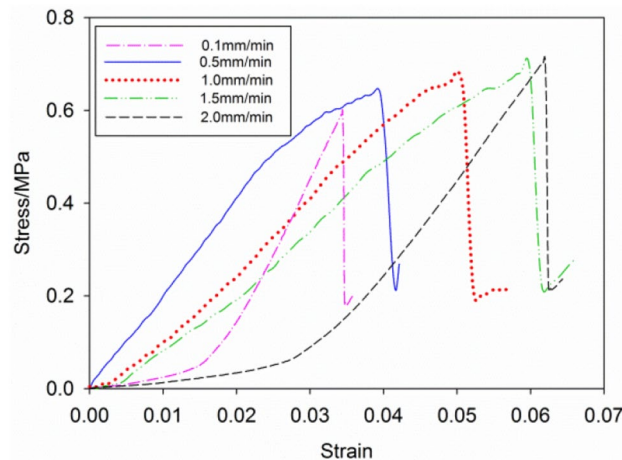


Fig. 10. Stress–strain curves of the foamed concrete at different loading rates.

cleavage loading process is not captured at high speed, even a uniform specimen often causes the illusion that cleavage damage starts from the edge.

Mechanical behavior and energy dissipation at different loading rates

For foamed concrete with a CNT content of 0.05%, a Brazilian splitting test with different loading rates was carried out. The loading rate of the testing machine was set to 0.1 mm/min, 0.5 mm/min, 1.0 mm/min, 1.5 mm/min, and 2.0 mm/min. The maximum loading time in this test was approximately 90 s, and the maximum strain value did not exceed 0.065. The maximum strain value did not exceed 0.065, which is much lower than the general dynamic loading strain rate, so the dynamic load effect is not considered in the test. Figure 10 shows the stress–strain curve of the specimen at five different loading rates. The tensile strength and ultimate strain of the specimens increased with increasing loading rate, and the stress–strain curve showed a nearly vertical drop after the peak. This finding showed that the foamed concrete specimen exhibited a certain degree of brittleness, and the end of the curve after each peak also had a phenomenon of “backlash”.

As shown in Fig. 11, the peak strength values of the specimen corresponding to different loading rates are extracted, and the data are fitted. The peak strength of the specimen had a logarithmic function relationship with the loading rate, as shown in Eq. (5):

$$\sigma_t = 0.686 + 0.0417 \ln \nu \quad R = 0.989 \quad (5)$$

where σ_t is the splitting tensile peak strength, ν is the loading rate, and R is the correlation coefficient. Because the “backlash” curve after the peak is the structural bearing stage after splitting, the ultimate strain is not included in the calculation. The bottom strain of the “backlash” is used as the limit strain of the specimen, and the limit strain of the specimen corresponding to different loading rates is extracted, as shown in Fig. 12. By fitting the data, it is found that the limit strain and the loading rate show a power function relationship, as shown in Eq. (6):

$$\sigma_t = 0.0537\nu^{0.2247} \quad R = 0.968 \quad (6)$$

The stress and strain values of the specimen increase with increasing loading rate. When the loading rate is low, sufficient time conditions are provided for the initiation, expansion, coalescence, and slip of the internal

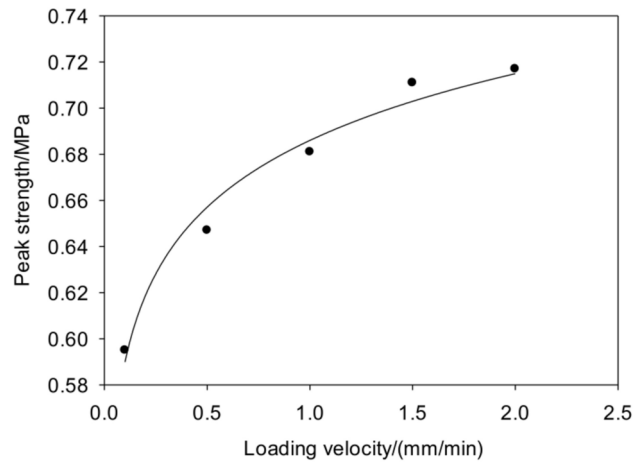


Fig. 11. Peak strength fitting.

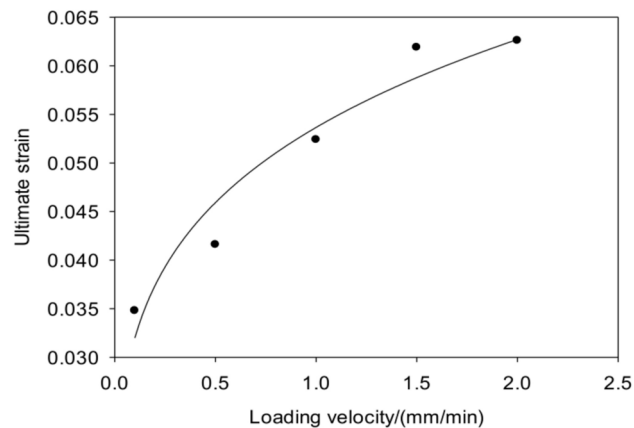


Fig. 12. Limit strain fitting.

cracks in the specimen. This series of processes can be achieved without applying excessive external loads to cause extreme specimen deformation. In the case of higher loading rates, the cracks generated inside the specimen do not have time to converge, and they tend to cement at the original initiation location and fail due to external force, resulting in forced expansion failure. Hence, under higher loading rates, the material must absorb a greater amount of external energy to facilitate the propagation of internal cracks and ultimately lead to failure. Moreover, the larger the external load is, the larger the corresponding deformation. The deformation and damage image information of the specimen with loading rates of 0.5 mm/min and 1.5 mm/min are extracted and shown in Fig. 13 and Fig. 14, respectively. A comparison of Fig. 13(a) and Fig. 14(a) shows that the specimens subjected lower loading rate exhibit a more ductile failure mode, characterized by more extensive deformation before ultimate failure. Conversely, at higher loading rates, the damage accumulation and crack propagation occur more rapidly, leading to a more abrupt and less ductile failure. Conversely, at higher loading rates, the damage accumulation and crack propagation occur more rapidly, leading to a more abrupt and less ductile failure. As shown in Fig. 13(b) and Fig. 14(b), the initial concentration of the maximum shear strain is 9×10^{-3} , and the loading rate has little effect on the sample. As shown in Fig. 13(c) and Fig. 14(c), it is obvious that the maximum shear strain value of the specimen at a high loading rate (0.12) is greater than that at a low loading rate (0.045). Furthermore, Fig. 13(d) and Fig. 14(d) show that the specimens with a high loading rate have more fracture-derived cracks, whereas the specimens with a low strain rate are collected into a macrocrack, which is consistent with the previous analysis.

From the perspective of energy, the energy dissipation characteristics of the modified foamed concrete under different loading rates are analyzed. Based on the energy dissipation curves presented in Fig. 15, it is evident that the failure characteristics at 0.1 mm/min and 2.0 mm/min differ from those at 0.5 mm/min, 1.0 mm/min, and 1.5 mm/min. This observation aligns with the understanding that different loading rates can lead to varying degrees of energy dissipation and failure modes in foamed concretes. At these moderate loading rates, the energy dissipation curves show a similar trend, indicating a comparable degree of energy absorption and dissipation. This could be attributed to the material's ability to undergo more extensive deformation before failure, allowing for a more uniform distribution of energy dissipation across the specimen. The energy consumption curves

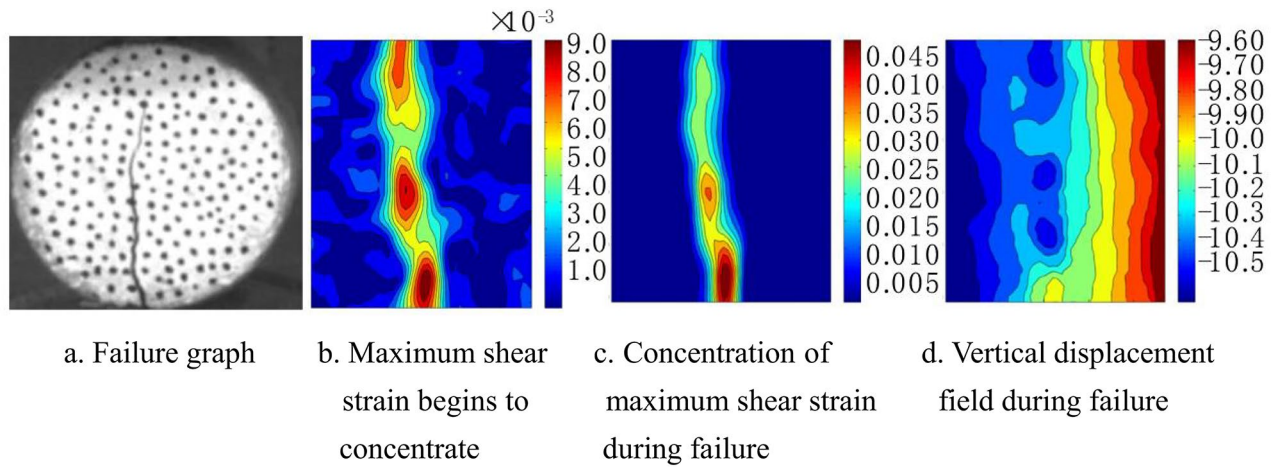


Fig. 13. Deformation and failure of the foamed concrete at a loading rate of 0.5 mm/min.

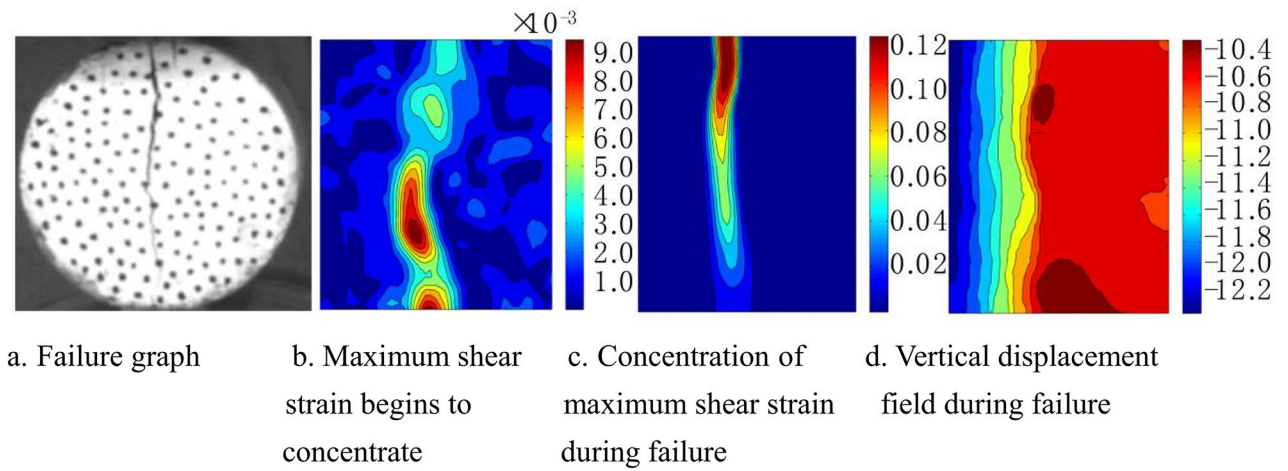


Fig. 14. Deformation and failure of the foamed concrete at a loading rate of 1.5 mm/min.

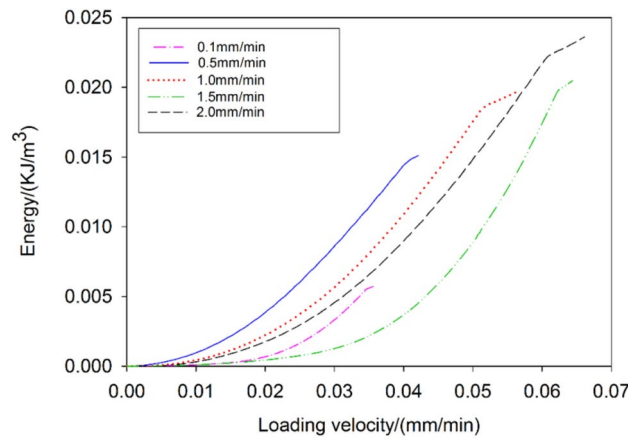


Fig. 15. Energy dissipation curves at different loading rates.

at these extreme rates exhibit different characteristics. The lower rate (0.1 mm/min) may show higher energy dissipation due to the material's ability to deform more extensively before failure, while the higher rate (2.0 mm/min) could result in a more abrupt failure with less energy dissipation, as there is less time for the material to absorb and distribute the energy. The distinct failure characteristics at 0.1 mm/min and 2.0 mm/min can be further explained by the material's response to different strain rates. At 0.1 mm/min, the material has more time to undergo deformation and energy absorption, leading to a higher energy dissipation capacity. Conversely, at 2.0 mm/min, the rapid application of load may lead to a more brittle failure with less energy dissipation, as the material has less time to absorb and distribute the energy effectively.

Conclusion

- 1) As the CNT content increases, the splitting tensile strength of the foamed concrete increases significantly. Considering the cost of CNTs, a CNT content of 0.05% is considered the optimal amount. On average, the addition of CNTs increased the peak strength of the foamed concrete by 67.2% and the ultimate strain by 21.7%, thus meeting the mechanical performance criteria for backfilling and mining operations.
- 2) A normalization method was used to identify the characteristic points on the stress–strain curve of the foamed concrete before and after modification, in terms of its splitting tensile strength. A comparative analysis of the horizontal strain field shows that the modified foamed concrete specimen is less likely to have a strain concentration area before reaching the peak strength and has a stronger resistance to deformation.
- 3) Under uniform conditions, the crack expansion starts in the central area of the specimen, and the crack expansion process goes through the cumulative deformation phase, the stable crack expansion phase, and the tensile cracking phase. After splitting, the foamed concrete specimen forms a transient triangular stable loadbearing structure, resulting in an increase in stress during continuous deformation. The structure is then crushed by the testing machine, which is the main reason for the “backlash” phenomenon at the end of each stress–strain curve.
- 4) The peak strength and ultimate strain of the CNT-modified foamed concrete exhibit distinct relationships with the loading rate, with the peak strength following a logarithmic function and the ultimate strain adhering to a power function. The energy dissipation behavior varies significantly at extreme loading rates of 0.1 mm/min and 2.0 mm/min compared to moderate rates of 0.5 mm/min, 1.0 mm/min, and 1.5 mm/min. At lower loading rates, the specimens demonstrate higher energy dissipation due to increased deformation capacity, while at higher rates, the energy dissipation is reduced due to the limited time for deformation and energy absorption. These observations highlight the influence of loading rate on the mechanical response and energy dissipation mechanisms of the modified foamed concrete.

In summary, this study presents a thorough investigation into the effects of carbon nanotubes (CNTs) on the mechanical properties of foamed concrete backfill, with a particular focus on splitting tensile strength. We have demonstrated that the incorporation of 0.05% CNTs by weight of cementitious materials significantly enhances the peak strength and ultimate strain of the foamed concrete backfill, with an average increase of 67.2% and 21.7%, respectively. The study also highlights the importance of the loading rate on the stress–strain behavior and energy dissipation characteristics of the modified foamed concrete. Our findings underscore the potential of CNT-modified foamed concrete as a high-performance backfill material for mining applications, offering improved mechanical stability and environmental benefits through the use of fly ash. The insights gained from this research contribute to the broader understanding of nanomaterial-modified construction materials and their practical applications in the field of civil engineering.

Data availability

Data will be made available on request. The first author should be contacted if someone wants to request the data from this study.

Received: 19 October 2024; Accepted: 30 December 2024

Published online: 14 January 2025

References

1. Wang, K., Li, K., Huang, X., Ni, W. & Zhang, S. Preparation of backfill materials by solidifying municipal solid waste incineration fly ash with slag-based cementitious materials. *Int. J. Environ. Sci. Technol.* **20**, 2745–2756 (2023).
2. Ma, Z. et al. Research on dynamic mechanical properties of polypropylene fiber-modified rubber foamed concrete. *Constr. Build. Mater.* **404**, 133282 (2023).
3. Beskopylny, A. N. et al. Improved fly ash based structural foam concrete with polypropylene fiber. *J. Compos. Sci.* **7**(2), 76 (2023).
4. Mydin, M. A. O. et al. Thermal conductivity, microstructure and hardened characteristics of foamed concrete composite reinforced with raffia fiber. *J. Mater. Res. Technol.* **26**, 850–864 (2023).
5. Shi, X., Ning, B., Na, F., Zhao, W. & Zhang, C. Study on properties of re-dispersible latex powder and polypropylene fiber-reinforced lightweight foam concrete. *J. Build. Eng.* **95**, 110156 (2024).
6. Shi, X., Ning, B., Liu, J. & Wei, Z. Effects of re-dispersible latex powder-basalt fibers on the properties and pore structure of lightweight foamed concrete. *J. Build. Eng.* **75**, 106984 (2023).
7. Zhang, Y. & Zheng, Y. Macro-mesoscale mechanical properties of basalt-polyvinyl alcohol hybrid fiber-reinforced low-heat portland cement concrete. *Polymers* **15**(3), 621 (2023).
8. Ahmed, T. et al. Utilization of novel basalt fiber pellets from micro-to macro-scale, and from basic to applied fields: A review on recent contributions. *Fibers* **12**(2), 17 (2024).
9. Wang, Q., Yao, B. & Lu, R. Behavior deterioration and microstructure change of polyvinyl alcohol fiber-reinforced cementitious composite (PVA-ECC) after exposure to elevated temperatures. *Materials* **13**(23), 5539 (2020).

10. Wang, J. et al. Understanding the effect of nano/micro-structures on anti-impact of nano-boron nitride filled cementitious composites. *Constr. Build. Mater.* **298**, 123885 (2021).
11. Meng, T., Ying, K., Yang, X. & Hong, Y. Comparative study on mechanisms for improving mechanical properties and microstructure of cement paste modified by different types of nanomaterials. *Nanotechnol. Rev.* **10**(1), 370–384 (2021).
12. Zhang, P., Su, J., Guo, J. & Hu, S. Influence of carbon nanotube on properties of concrete: A review. *Constr. Build. Mater.* **369**, 130388 (2023).
13. Liu, J., Li, Y., Jin, C., Lin, H. & Li, H. Effect and mechanism analysis of hydroxylated nano-boron nitride on workability and multi-scale mechanical properties of cement paste. *Arch. Civil Mech. Eng.* **22**(3), 122 (2022).
14. Onaizi, A. M. et al. Towards increased adoption of furnace bottom ash as sustainable building materials: Characterization, standardization, and applications. *J. Build. Eng.* **82**, 108274 (2023).
15. Hung, C. C., Chen, Y. T. & Yen, C. H. Workability, fiber distribution, and mechanical properties of UHPC with hooked end steel macro-fibers. *Constr. Build. Mater.* **260**, 119944 (2020).
16. Hao, Y., Yang, G. & Liang, K. Development of fly ash and slag based high-strength alkali-activated foam concrete. *Cement Concr. Compos.* **128**, 104447 (2022).
17. Tran, N. P., Nguyen, T. N., Ngo, T. D., Le, P. K. & Le, T. A. Strategic progress in foam stabilisation towards high-performance foam concrete for building sustainability: A state-of-the-art review. *J. Clean. Prod.* **375**, 133939 (2022).
18. Li, X. & Xu, Y. Phase field modeling scheme with mesostructure for crack propagation in concrete composite. *Int. J. Solids Struct.* **234**, 111259 (2022).
19. Jiang, Z., Zhu, Z. & Accornero, F. Tensile-to-shear crack transition in the compression failure of steel-fibre-reinforced concrete: insights from acoustic emission monitoring. *Buildings* **14**(7), 2039 (2024).
20. Shahpari, M., Bamonte, P. & Mosallam, S. J. An experimental study on mechanical and thermal properties of structural lightweight concrete using carbon nanotubes (CNTs) and LECA aggregates after exposure to elevated temperature. *Constr. Build. Mater.* **346**, 128376 (2022).
21. Abd Elrahman, M., Sikora, P., Chung, S. Y. & Dstephan, D. The performance of ultra-lightweight foamed concrete incorporating nanosilica. *Arch. Civil Mech. Eng.* **21**(2), 79 (2021).
22. Sldozian, R. J., Burakov, A. E., Aljaboobi, D. Z. M., Hamad, A. J. & Tkachev, A. G. The effect of multi-walled carbon nanotubes on mechanical properties and water adsorption of lightweight foamed concrete. *Res. Eng. Struct. Mater.* **10**(3), 1139–1154 (2024).
23. Yu, X., Zuo, J., Mao, L., Li, Y. & Yang, L. Crack propagation behavior and failure prediction of rocks with non-parallel conjugate flaws: Insights from the perspective of acoustic emission and DIC. *Theor. Appl. Fract. Mech.* **134**, 104709 (2024).
24. Hou, Z., Yuan, R., Chen, Y. & Sun, W. Crack propagation process in double-flawed granite under compression using digital image correlation method and numerical simulation. *Sci. Rep.* **14**(1), 21424 (2024).

Acknowledgements

The authors acknowledge the support of the project ZR2024ME257 supported by Shandong Provincial Natural Science Foundation. Additionally, the authors thank American Journal Experts [www.aje.com] for providing English-language editing.

Author contributions

Shukun Zhang: Conceptualization, Methodology, Funding acquisition. Xinghui Wu: Validation, Writing–review & editing. Peng Jiang: Conceptualization, Methodology, Writing–review & editing. Haohao Wang: Conceptualization, Methodology, Data curation. Shuai Wang: Writing–original draft, Project administration. Haojie Yang: Investigation, Data curation. Lu Lu: Writing–original draft, Visualization.

Funding

Natural Science Foundation of Shandong Province, ZR2024ME257.

Declarations

Competing interest

We declare that we do not have any commercial or associative interest that represents a conflict of interest in connection with the work submitted.

Additional information

Correspondence and requests for materials should be addressed to X.W.

Reprints and permissions information is available at www.nature.com/reprints.

Publisher's note Springer Nature remains neutral with regard to jurisdictional claims in published maps and institutional affiliations.

Open Access This article is licensed under a Creative Commons Attribution-NonCommercial-NoDerivatives 4.0 International License, which permits any non-commercial use, sharing, distribution and reproduction in any medium or format, as long as you give appropriate credit to the original author(s) and the source, provide a link to the Creative Commons licence, and indicate if you modified the licensed material. You do not have permission under this licence to share adapted material derived from this article or parts of it. The images or other third party material in this article are included in the article's Creative Commons licence, unless indicated otherwise in a credit line to the material. If material is not included in the article's Creative Commons licence and your intended use is not permitted by statutory regulation or exceeds the permitted use, you will need to obtain permission directly from the copyright holder. To view a copy of this licence, visit <http://creativecommons.org/licenses/by-nc-nd/4.0/>.

© The Author(s) 2024